Computing 75, 197–213 (2005)
Digital Object Identifier (DOI) 10.1007/s00607-004-0095-x

Computing
Printed in Austria

Numerical Recovery of Conductivity at the Boundary from the Localized Dirichlet to Neumann Map

G. Nakamura, Sapporo, **S. Siltanen,** Helsinki, **K. Tanuma,** Kiryu, and **S. Wang,** Sapporo

Received December 20, 2003; revised July 2, 2004
Published online: December 8, 2004

Abstract

Numerical implementation of the reconstruction formulae of Nakamura and Tanuma [Recent Development in Theories and Numerics, International Conference on Inverse Problems 2003] is presented. With the formulae, the conductivity and its normal derivative can be recovered on the boundary of a planar domain from the localized Dirichlet to Neumann map. Such reconstruction method is needed as a preliminary step before full reconstruction of conductivity inside the domain from boundary measurements, as done in electrical impedance tomography. Properties of the method are illustrated with reconstructions from simulated data.

AMS Subject Classifications: 31A25, 15A29.

Keywords: Electrical impedance tomography, boundary determination, localized Dirichlet to Neumann map, inverse conductivity problem.

1. Introduction

Electrical impedance tomography (EIT) is an emerging medical imaging method, where the conductivity distribution inside the body is reconstructed from electrical measurements on the skin. Possible applications include monitoring heart and lung function of unconscious patients, diagnosis of pulmonary edema, and detection of breast cancer. For overview of EIT see [8], [2], [3], and for a discussion of medical applications see [4]. In this paper we present a new numerical method for determining the conductivity and its normal derivative at the boundary of the body from local measurements. This is a preliminary step before full reconstruction.

The mathematical formulation of EIT is the inverse conductivity problem first posed by Calderón [7]. Let $\Omega \subset \mathbb{R}^d$ with $d = 2$ or $d = 3$ be a bounded set with Lipschitz boundary. Given a strictly positive, real-valued conductivity $\gamma \in L^\infty(\Omega)$, we apply a voltage potential f on the boundary and solve the Dirichlet problem

$$\nabla \cdot \gamma \nabla u = 0 \quad in\ \Omega, \qquad u = f \quad on\ \partial\Omega, \tag{1.1}$$

where $u(x)$ is electric voltage potential. The resulting current density distribution is

$$\Lambda_\gamma f = \gamma \frac{\partial u}{\partial v}|_{\partial\Omega}. \tag{1.2}$$

The physical interpretation of the Dirichlet-to-Neumann (DN) map Λ_γ is knowledge of the resulting current distributions on the boundary of Ω corresponding to all possible voltage distributions on the boundary. (We note that often in practice currents are applied and voltages measured.) Thus, the problem we are concerned with is to determine γ from Λ_γ.

A brief review of some of the previous works is as follows. When γ and $\partial\Omega$ are C^∞, using the fact that Λ_γ is a pseudo-differential operator, Sylvester and Uhlmann [24] showed how to recover γ and all of its derivatives on $\partial\Omega$ from the symbol of Λ_γ. When $\partial\Omega$ is Lipschitz continuous, from Λ_γ Nachman [17] recovered γ on $\partial\Omega$ if $\gamma \in W^{1,p}(\Omega)$ with $p > d$ and recovered the first normal derivative of γ on $\partial\Omega$ if $\gamma \in W^{2,p}(\Omega)$ with $p > d/2$. Then a procedure to reconstruct γ in Ω was also given. Quite recently, in the case where $\Omega \subset \mathbb{R}^2$, Astala and Päivärinta [1] reconstructed γ in Ω only under the assumption that $\gamma \in L^\infty(\Omega)$.

We are interested in reconstructing γ and its normal derivative at the boundary $\partial\Omega$ from the localized Λ_γ. More precisely: for $x_0 \in \partial\Omega$, assuming certain regularity conditions on γ and on $\partial\Omega$ locally around x_0, one inputs Dirichlet data f which are compactly supported in a neighborhood of x_0 on $\partial\Omega$, measures corresponding Neumann data $\Lambda_\gamma f$ in that neighborhood, and then reconstructs $\gamma(x_0)$ and $\partial\gamma/\partial v(x_0)$. Earlier works on reconstruction from the localized Λ_γ include [5], [12], [17], [18], [19], [20], [21]. Each reconstruction formula obtained there has its own advantage. For example, a weaker assumption on the regularity of γ in [5], reconstruction of higher-order derivatives of γ in [12], [18], and simultaneous reconstruction of γ and its normal derivative in [19]. However, to our knowledge, there are no previous numerical implementations of theoretical boundary determination formulae.

The main application of numerical boundary reconstruction is to provide a missing part for EIT algorithms of the following types: (a) methods for the linearized problem, (b) iterative cost-function minimization methods, and (c) $\overline{\partial}$ methods. (See [2], [3] for a detailed review of EIT algorithms.) We briefly describe the benefits of our results for each type of methods. Algorithms of type (a) are designed for conductivities that are small perturbations of a known background. In practice, the background is not known but needs to be estimated, and knowledge of $\gamma|_{\partial\Omega}$ and $\partial\gamma/\partial v|_{\partial\Omega}$ is helpful. Methods of type (b) aim to minimize a nonlinear and non-convex functional, so a good initial guess for γ in $\overline{\Omega}$, in particular on $\partial\Omega$, is needed to avoid local minima. Methods of type (c) are regularized implementations of the uniqueness proofs of Nachman [17] or Brown and Uhlmann [6], both of which are based on the $\overline{\partial}$ method of inverse scattering. Such implementations are described in [22], [16], [11], [13], [15], [14]. However, in the numerical works it was assumed that γ is constant near the boundary. This

assumption is rather unnatural, and in fact the general situation is reduced in [17], [6] to that case as follows. First, recover $\gamma|_{\partial\Omega}$ and $\partial\gamma/\partial\nu|_{\partial\Omega}$ (in the approach of Brown and Uhlmann, the derivative is not needed); second, continue γ artificially outside Ω to a larger bounded set Ω' satisfying $\overline{\Omega} \subset \Omega'$ so that γ' is in an appropriate Sobolev space and $\gamma' \equiv 1$ near $\partial\Omega'$; third, recover $\Lambda_{\gamma'}$ from the knowledge of Λ_γ.

In this paper, we present numerical implementations for the reconstruction formulae of Nakamura and Tanuma [20]. For simplicity we take $\Omega \subset \mathbb{R}^2$ to be the unit disc, although the presented methods cover the three-dimensional case and more general domains. According to [20], [21], we can recover the trace $\gamma|_{\partial\Omega}$ and normal derivative $\partial\gamma/\partial\nu|_{\partial\Omega}$ of a C^1 conductivity γ in weak form with the formulae

$$\int_{\partial\Omega} \gamma\eta^2 d\sigma = \lim_{N\to\infty} N^{-1} \int_{\partial\Omega} \overline{\phi_N} \Lambda_\gamma \phi_N d\sigma, \tag{1.3}$$

$$\int_{\partial\Omega} \frac{\partial\gamma}{\partial\nu} \eta^2 d\sigma = \lim_{N\to\infty} \int_{\partial\Omega} \left(4\overline{\psi_N}\Lambda_\gamma\psi_N - 2\overline{\phi_N}\Lambda_\gamma\phi_N\right) d\sigma, \tag{1.4}$$

where $d\sigma$ is the surface measure on the boundary, $\eta \in C_0^1(\partial\Omega)$ is a smooth, compactly supported function satisfying $\int_{\partial\Omega} \eta^2(\theta)d\theta = 1$, and the functions ϕ_N and ψ_N are given by

$$\phi_N(\theta) = e^{iN\theta}\eta(\theta), \qquad \psi_N(\theta) = e^{i\frac{N}{2}\theta}\eta(\theta),$$

where $i = \sqrt{-1}$ and we parametrize the unit circle as

$$\partial\Omega = \{(\cos\theta, \sin\theta) \in \mathbb{R}^2 | -\pi \le \theta < \pi\}.$$

Our reconstruction algorithm consists essentially of evaluating the right-hand sides of (1.3) and (1.4) with a finite N.

In practical EIT, voltages are applied on (or currents injected to) the body using a finite number of electrodes. We take electrode measurements into account in a rather simple way: we apply continuous voltage potentials ϕ_N and ψ_N at the boundary, but keep N small enough for the spatial oscillations of ϕ_N and ψ_N roughly realizable by a practically feasible number of electrodes. More involved electrode models are discussed in [9], [23].

A shortcoming of our approach is that we can only recover blurred versions of the functions $\gamma|_{\partial\Omega}$ and $\partial\gamma/\partial\nu|_{\partial\Omega}$. Our method could be complemented with a deblurring method, such as Tikhonov or total variation regularization, see [25]. However, we view deblurring as an independent postprocessing step and do not discuss it in this paper.

This paper is organized as follows. In Sect. 2, we write the results in [20] in a form suitable for Ω being the unit disc. In Sect. 3, we discuss numerical techniques for the implementation of the reconstruction formulae and the simulation of noisy data. In Sect. 4, we present numerical examples. We discuss our results in Sect. 5.

2. Reconstruction Formulae

Formulae (1.3) and (1.4) are obtained from the method of coordinate transformation in [18] and Theorem 4 in [20]. We note that formula (1.4) does not involve the trace of γ. Hence we do not need any information about the values of γ in the support of η when reconstructing (a weak form of) the normal derivative of γ there. This gives an efficient method for numerical realization. Now we will give a brief sketch of a derivation of formulae (1.3) and (1.4).

Let (x_1, x_2) be a Cartesian coordinate system so that

$$\Omega = \{(x_1, x_2) \mid x_1^2 + x_2^2 \leq 1\}, \quad \partial\Omega = \{(x_1, x_2) \mid x_1^2 + x_2^2 = 1\}.$$

We introduce a new coordinate system (θ, r) by

$$x_1 = (1 - r)\cos\theta, \qquad x_2 = (1 - r)\sin\theta. \tag{2.1}$$

Then Ω and $\partial\Omega$ are given by $0 < r \leq 1$ and $r = 0$, respectively, $(-\pi \leq \theta < \pi)$. Transformation (2.1) induces a C^1 diffeomorphism $F : (x_1, x_2) \longrightarrow (\theta, r)$ on $\Omega \setminus \{0\}$, whose gradient ∇F and Jacobian $J = \det \nabla F$ are given by

$$\nabla F = \begin{pmatrix} -\sin\theta/(1-r) & \cos\theta/(1-r) \\ -\cos\theta & -\sin\theta \end{pmatrix}, \quad J = \frac{1}{1-r}. \tag{2.2}$$

Put

$$\Phi_N = e^{iN\theta}\eta(\theta)e^{-Nr}.$$

Then $\Phi_N(F(x))$ is an $H^1(\Omega)$-extension of the function $\phi_N(F(x)) \in H^1(\partial\Omega)$. Now from Green's function and the change of the coordinate system it follows that

$$\begin{aligned} \int_{\partial\Omega} (\Lambda_\gamma \phi_N)\overline{\phi_N} d\sigma &= \int_\Omega \gamma \nabla u_N \cdot \nabla \overline{\Phi_N(F(x))}\, dx \\ &= \int_{-\pi}^{\pi} \int_0^1 \left(\widetilde{\gamma} \nabla_{\theta,r} u_N\right) \cdot \nabla_{\theta,r} \overline{\Phi_N}\, dr d\theta, \end{aligned} \tag{2.3}$$

where $u_N \in H^1(\Omega)$ is the solution to

$$\nabla \cdot \gamma \nabla u_N = 0 \quad \text{in} \quad \Omega, \qquad u_N|_{\partial\Omega} = \phi_N(F(x)) \tag{2.4}$$

and $\widetilde{\gamma} = \widetilde{\gamma}(\theta, r)$ is a 2×2 matrix defined by

$$\widetilde{\gamma}(\theta, r) = J^{-1} \nabla F (\nabla F)^T \gamma. \tag{2.5}$$

Noting that (2.4) is equivalent to

$$\nabla_{\theta,r} \cdot \widetilde{\gamma} \nabla_{\theta,r} u_N = 0 \quad \textit{in} \quad [-\pi, \pi] \times [0, 1], \qquad u_N|_{r=0} = \phi_N, \tag{2.6}$$

we observe that $\Phi_N(F(x))$ is the first term of an asymptotic solution to (2.4) for large N. In fact, from

$$\nabla_{\theta,r}\Phi_N = N\begin{pmatrix} i \\ -1 \end{pmatrix} e^{iN\theta}\eta(\theta)e^{-Nr} + \begin{pmatrix} \eta'(\theta) \\ 0 \end{pmatrix} e^{iN\theta}e^{-Nr} \tag{2.7}$$

and $\begin{pmatrix} i \\ -1 \end{pmatrix} \cdot \begin{pmatrix} i \\ -1 \end{pmatrix} = 0$ we see that Φ_N satisfies (2.6) in the order N^2. Hence it can be proved ([21]) that the leading term of (2.3) in N for large N is obtained by replacing u_N with Φ_N. That is, we have

$$\int_{\partial\Omega} (\Lambda_\gamma \phi_N)\overline{\phi_N} d\sigma \sim \int_{-\pi}^{\pi}\int_0^1 (\tilde{\gamma}\nabla_{\theta,r}\Phi_N)\cdot\nabla_{\theta,r}\overline{\Phi_N}\, dr d\theta.$$

Here and hereafter we use the notation $\sim$ to indicate that we are retaining the leading term in N for large N and are neglecting the higher-order terms. Thus, from (2.7) we get

$$N^{-1}\int_{\partial\Omega} (\Lambda_\gamma \phi_N)\overline{\phi_N} d\sigma \sim N\int_{-\pi}^{\pi}\int_0^1 \tilde{\gamma}(\theta, r)\begin{pmatrix} i \\ -1 \end{pmatrix}\cdot\begin{pmatrix} -i \\ -1 \end{pmatrix} e^{-2Nr}\eta(\theta)^2\, dr d\theta,$$

and after the scaling transformation

$$R = Nr \tag{2.8}$$

we get

$$\sim \int_{-\pi}^{\pi}\int_0^N \tilde{\gamma}(\theta, \frac{R}{N})\begin{pmatrix} i \\ -1 \end{pmatrix}\cdot\begin{pmatrix} -i \\ -1 \end{pmatrix} e^{-2R}\eta(\theta)^2\, dR d\theta.$$

By Lebesgue's dominated convergence theorem, this tends to

$$\frac{1}{2}\int_{-\pi}^{\pi}\tilde{\gamma}(\theta, 0)\begin{pmatrix} i \\ -1 \end{pmatrix}\cdot\begin{pmatrix} -i \\ -1 \end{pmatrix}\eta(\theta)^2\, d\theta$$

as N goes to infinity. Since (2.2) and (2.5) imply that

$$\tilde{\gamma}(\theta, r) = \begin{pmatrix} 1/(1-r) & 0 \\ 0 & 1-r \end{pmatrix}\gamma, \tag{2.9}$$

we immediately obtain (1.3).

Let Ψ_N be an $H^1(\Omega)$-extension of the function ψ_N of the form

$$\Psi_N = e^{i\frac{N}{2}\theta}\eta(\theta)e^{-\frac{N}{2}r}.$$

Then in the same way as (2.3), it follows that

$$\int_{\partial\Omega} 4(\Lambda_\gamma \psi_N)\overline{\psi_N} - 2(\Lambda_\gamma \phi_N)\overline{\phi_N} d\sigma$$
$$= \int_\Omega \gamma\Big(4\nabla v_N \cdot \nabla\overline{\Psi_N(F(x))} - 2\nabla u_N \cdot \nabla\overline{\Phi_N(F(x))}\Big)dx$$
$$= \int_{-\pi}^{\pi}\int_0^1 4\big(\widetilde{\gamma}\nabla_{\theta,r} v_N\big)\cdot\nabla_{\theta,r}\overline{\Psi_N} - 2\big(\widetilde{\gamma}\nabla_{\theta,r} v_N\big)\cdot\nabla_{\theta,r}\overline{\Phi_N}\ dr d\theta,$$

where $v_N \in H^1(\Omega)$ is the solution to

$$\nabla\cdot\gamma\nabla v_N = 0 \quad in \quad \Omega, \qquad v_N|_{\partial\Omega} = \psi_N(F(x)), \tag{2.10}$$

and u_N and Φ_N are the same as in before. From

$$\nabla_{\theta,r}\Psi_N \sim \frac{N}{2}\begin{pmatrix} i \\ -1\end{pmatrix} e^{i\frac{N}{2}\theta}\eta(\theta)e^{-\frac{N}{2}r} + \begin{pmatrix}\eta'(\theta)\\ 0\end{pmatrix} e^{i\frac{N}{2}\theta}e^{-\frac{N}{2}r} \tag{2.11}$$

we also observe that $\Psi_N(F(x))$ is the first term of an asymptotic solution to (2.10) for large N. Therefore, we obtain

$$\int_{\partial\Omega} 4(\Lambda_\gamma \psi_N)\overline{\psi_N} - 2(\Lambda_\gamma \phi_N)\overline{\phi_N} d\sigma$$
$$\sim \int_{-\pi}^{\pi}\int_0^1 4\big(\widetilde{\gamma}\nabla_{\theta,r}\Psi_N\big)\cdot\nabla_{\theta,r}\overline{\Psi_N} - 2\big(\widetilde{\gamma}\nabla_{\theta,r}\Phi_N\big)\cdot\nabla_{\theta,r}\overline{\Phi_N}\ dr d\theta,$$

and from (2.7) and (2.11) we get

$$\sim N^2\int_{-\pi}^{\pi}\int_0^1 \widetilde{\gamma}(\theta,r)\begin{pmatrix} i\\ -1\end{pmatrix}\cdot\begin{pmatrix}-i\\ -1\end{pmatrix}\big(e^{-Nr} - 2e^{-2Nr}\big)\eta(\theta)^2\ dr d\theta.$$

Then integration by parts in r and the scaling transformation (2.8) lead to

$$\int_{\partial\Omega} 4(\Lambda_\gamma \psi_N)\overline{\psi_N} - 2(\Lambda_\gamma \phi_N)\overline{\phi_N} d\sigma$$
$$\sim N\int_{-\pi}^{\pi}\int_0^1 \frac{\partial}{\partial r}\widetilde{\gamma}(\theta,r)\begin{pmatrix} i\\ -1\end{pmatrix}\cdot\begin{pmatrix}-i\\ -1\end{pmatrix}\big(e^{-Nr} - e^{-2Nr}\big)\eta(\theta)^2\ dr d\theta$$
$$= \int_{-\pi}^{\pi}\int_0^N \frac{\partial\widetilde{\gamma}}{\partial r}(\theta,\frac{R}{N})\begin{pmatrix} i\\ -1\end{pmatrix}\cdot\begin{pmatrix}-i\\ -1\end{pmatrix}\big(e^{-R} - e^{-2R}\big)\eta(\theta)^2\ dR d\theta.$$

By Lebesgue's bounded convergence theorem, the last integral tends to

$$\frac{1}{2}\int_{-\pi}^{\pi}\frac{\partial\widetilde{\gamma}}{\partial r}(\theta,0)\begin{pmatrix} i\\ -1\end{pmatrix}\cdot\begin{pmatrix}-i\\ -1\end{pmatrix}\eta(\theta)^2\ d\theta \tag{2.12}$$

as N goes to infinity. Also, from (2.9) it follows that

$$\frac{\partial \widetilde{\gamma}}{\partial r}(\theta, 0) = \begin{pmatrix} 1 & 0 \\ 0 & -1 \end{pmatrix} \gamma|_{\partial\Omega} + \begin{pmatrix} 1 & 0 \\ 0 & 1 \end{pmatrix} \frac{\partial \gamma}{\partial r}\Big|_{\partial\Omega}.$$

Therefore, noting that

$$\begin{pmatrix} 1 & 0 \\ 0 & -1 \end{pmatrix} \begin{pmatrix} i \\ -1 \end{pmatrix} \cdot \begin{pmatrix} -i \\ -1 \end{pmatrix} = 0 \quad \textit{and} \quad \begin{pmatrix} 1 & 0 \\ 0 & 1 \end{pmatrix} \begin{pmatrix} i \\ -1 \end{pmatrix} \cdot \begin{pmatrix} -i \\ -1 \end{pmatrix} = 2,$$

we obtain (1.4) from (2.12).

3. Numerical Methods

Let η be a smooth cutoff function supported in a neighborhood of the point $x_0 \in \partial\Omega$ corresponding to $\theta = 0$. Given a positive integer N and a point $x = (\beta, 0) \in \partial\Omega$ with $-\pi \leq \beta < \pi$, we perform the following three steps to recover a blurred version of $\gamma|_{\partial\Omega}$ from the localized DN map.

First, we define

$$\phi_{N,\beta}(\theta) = e^{iN\theta}\eta(\theta - \beta) \tag{3.1}$$

and solve the boundary value problem

$$\begin{cases} \nabla \cdot (\gamma \nabla u_1) = 0 & \text{in } \Omega, \\ u_1 = \phi_{N,\beta} & \text{on } \partial\Omega, \end{cases}$$

with the finite element method (FEM). We use the "adaptmesh" solution routine of the FreeFEM++ software (version 1.32), see [10]. That routine constructs a mesh adapted to the second differentiated field of the prescribed function.

Second, we use finite differences to evaluate the expression

$$\Lambda_\gamma \phi_{N,\beta} := \gamma \frac{\partial u_1}{\partial r}|_{\partial\Omega}.$$

Third, we compute

$$g_N(\beta) := N^{-1} \int_{\partial\Omega} \overline{\phi_{N,\beta}} \Lambda_\gamma \phi_{N,\beta} d\sigma \tag{3.2}$$

with numerical integration. Further, we add simulated noise to our measurements by

$$\tilde{g}_N(\beta) := N^{-1} \int_{\partial\Omega} \overline{\phi_{N,\beta}} (\mathscr{E}_N + \Lambda_\gamma \phi_{N,\beta}) d\sigma, \tag{3.3}$$

where

$$\mathscr{E}_N(\theta) = \sum_{\ell=-N+1}^{N} a_\ell e^{i\ell\theta}, \tag{3.4}$$

and a_ℓ are independent normally distributed random variables with mean zero and standard deviation $\sigma = 0.0001 \cdot (2N)^{-1/2} \max_\theta |(\Lambda_\gamma \phi_{N,\beta})(\theta)|$. This models a noisy measurement with $2N$ electrodes and relative noise level 0.01%.

We consider $g_N(\beta)$ and $\tilde{g}_N(\beta)$ as approximations to the convolution

$$(\gamma|_{\partial\Omega} * \eta^2)(\beta) = \int_{\beta-\pi}^{\beta+\pi} \gamma|_{\partial\Omega}(\theta)\eta^2(\theta-\beta)d\theta.$$

We turn to the reconstruction of the normal derivative. First, we define

$$\psi_{N,\beta}(\theta) = e^{i\frac{N}{2}\theta}\eta(\theta-\beta) \tag{3.5}$$

and use FEM to solve the boundary value problem

$$\begin{cases} \nabla\cdot(\gamma\nabla u_2) = 0 & \text{in } \Omega, \\ u_2 = \psi_{N,\beta} & \text{on } \partial\Omega. \end{cases}$$

Second, we use finite differences to evaluate the expression

$$\Lambda_\gamma \psi_{N,\beta} := \gamma \frac{\partial u_2}{\partial r}|_{\partial\Omega}.$$

Third, we use numerical integration to compute

$$h_N(\beta) = \int_{\partial\Omega} \left(4\overline{\psi_{N,\beta}}\Lambda_\gamma\psi_{N,\beta} - 2\overline{\phi_{N,\beta}}\Lambda_\gamma\phi_{N,\beta}\right)d\sigma. \tag{3.6}$$

Again, we add noise by defining

$$\tilde{h}_N(\beta) = \int_{\partial\Omega} \left(4\overline{\psi_{N,\beta}}(\mathscr{E}_N + \Lambda_\gamma\psi_{N,\beta}) - 2\overline{\phi_{N,\beta}}(\mathscr{E}_N + \Lambda_\gamma\phi_{N,\beta})\right)d\sigma. \tag{3.7}$$

We consider $h_N(\beta)$ and $\tilde{h}_N(\beta)$ as approximations to the convolution

$$(\frac{\partial\gamma}{\partial r}|_{\partial\Omega} * \eta^2)(\beta) = \int_{\beta-\pi}^{\beta+\pi} \frac{\partial\gamma}{\partial r}|_{\partial\Omega}(\theta)\eta^2(\theta-\beta)d\theta.$$

4. Results

We discuss three numerical examples. In Sect. 4.1, we consider a simulated cross-section of the human chest and use simulated measurements to examine whether our approach can be used as the missing step in $\bar{\partial}$ reconstruction algorithms for

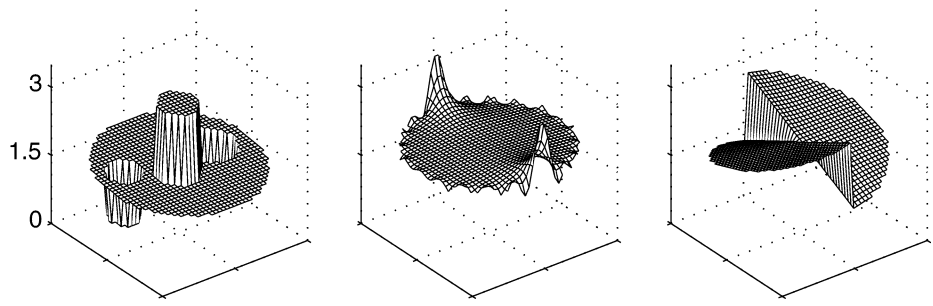

Fig. 1. Three example conductivities. Left: the conductivity γ is a rough model of a cross-section of the human chest. Middle: smooth conductivity γ' with relatively rapid changes at the boundary. Right: a discontinuous conductivity distribution γ''. Axis limits are the same in all the plots

EIT. In Sect. 4.2, we define a rapidly changing smooth conductivity and recover its trace and normal derivative. This way we examine the effect of the point spread function η^2 in the weak-form reconstruction. In Sect. 4.3, we make a numerical experiment with a conductivity having discontinuities. The reconstruction formulae (1.3) and (1.4) are not proven to hold near the points of discontinuity, but we expect to gain intuition by observing numerical results. See Fig. 1 for plots of the example conductivities.

The domain Ω is the unit disc in all the examples. We think of electrode configurations with $32, 64$ and 96 electrodes leading to the choices $N = 16, 32, 48$, respectively, since N is the maximum frequency of Dirichlet data we can express in (3.1) and (3.5) with $2N$ electrodes. For instance, the ACT3 EIT machine at Rensselaer Polytechnic Institute has 32 electrodes.

We use the following point spread function:

$$\eta(\theta) = \begin{cases} c(\epsilon\theta - \frac{\pi}{2})^{\alpha}(\epsilon\theta + \frac{\pi}{2})^{\alpha}\cos(\epsilon\theta) & \text{for } -\frac{\pi}{2\epsilon} < \theta < \frac{\pi}{2\epsilon}, \\ 0 & \text{otherwise,} \end{cases}$$

where $\epsilon = 4$ and $\alpha = 4$. The constant c is chosen so that $\int_{\partial\Omega} \eta^2(\theta)d\theta = 1$. See Fig. 2 for a plot of η^2.

In all finite element computations, we use the "adaptmesh" command of Freefem++ with initial error level 0.001, and in each loop we set the new error level to be the previous one multiplied by $0.1^{\frac{1}{20}}$.

4.1. Simulated Human Chest Phantom

We construct a conductivity distribution inside the unit disc that roughly models a cross-section of the human chest. Let the background conductivity be $\frac{3}{2}$ and introduce three circular inclusions. One inclusion models the heart and has conductivity 3. Two other inclusions model the lungs and have conductivity $\frac{1}{2}$.

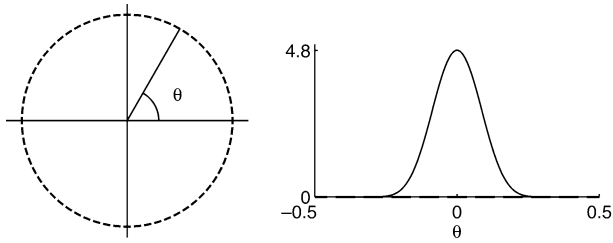

Fig. 2. Left: a configuration of 64 electrodes on the unit circle. Right: plot of the point spread function $\eta^2(\theta)$. The location of η^2 corresponds to reconstruction at $\theta = 0$. Note that in this case of 64 electrodes the support of η covers theoretically 8 but effectively 5 electrodes

Further, to make the conductivity nonconstant near the boundary, we add the function $2x_2/10$. So our chest phantom conductivity takes the form

$$\gamma(x_1, x_2) = \frac{3}{2} + \frac{2}{10}x_2 + \frac{3}{2}\chi_{D_1} - \chi_{D_2} - \chi_{D_3},$$

where $D_j \subset \Omega$ are the following non-overlapping discs:

$$D_1 = B\left(\left(-\frac{1}{10}, -\frac{1}{10}\right), \frac{1}{4}\right), \quad D_2 = B\left(\left(-\frac{6}{10}, \frac{1}{10}\right), \frac{1}{10}\right), \quad D_3 = B\left(\left(\frac{1}{2}, \frac{1}{10}\right), \frac{3}{10}\right).$$

See the left plot of Fig. 1. The trace and normal derivative of γ change so slowly that there is no big difference between the actual functions and convolved ones. Indeed, the relative $L^2(\partial\Omega)$ and $L^\infty(\partial\Omega)$ errors between them are very small, as seen by numerical computation:

$$\frac{\|\gamma - \gamma * \eta^2\|_{L^2(\partial\Omega)}}{\|\gamma\|_{L^2(\partial\Omega)}} \approx 0.0003, \qquad \frac{\|\partial\gamma/\partial r - (\partial\gamma/\partial r) * \eta^2\|_{L^2(\partial\Omega)}}{\|\partial\gamma/\partial r\|_{L^2(\partial\Omega)}} \approx 0.003,$$

$$\frac{\max_{\partial\Omega}|\gamma - \gamma * \eta^2|}{\max_{\partial\Omega}|\gamma|} \approx 0.0004, \qquad \frac{\max_{\partial\Omega}|\partial\gamma/\partial r - (\partial\gamma/\partial r) * \eta^2|}{\max_{\partial\Omega}|\partial\gamma/\partial r|} \approx 0.003.$$

We reconstruct $(\gamma|_{\partial\Omega} * \eta^2)(0) = 1.5$ and $(\partial\gamma/\partial r|_{\partial\Omega} * \eta^2)(0) = 0$ in weak form from the localized DN map by computing $g_N(0)$ and $h_N(0)$ for various N. The speed of convergence can be seen in Fig. 3.

We turn to weak-form reconstructions of $\gamma|_{\partial\Omega}$ and $\partial\gamma/\partial r|_{\partial\Omega}$ as functions. Thinking about the case of $2N$ electrodes, we reconstruct at $2N$ points of the circle boundary:

$$\beta_\ell = -\pi + \frac{\ell}{2N}2\pi, \qquad \ell = 0, 1, 2, \cdots, 2N - 1. \tag{4.1}$$

We introduce noisy data as explained in Sect. 3. We choose the relative noise level of 0.01% and compute the functions $\tilde{g}_N$ and $\tilde{h}_N$ with formulae (3.3) and (3.7), respectively. See the plots of these functions in Figs. 4 and 5.

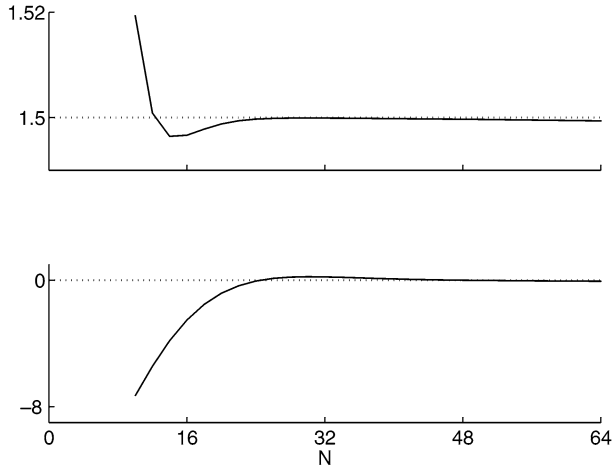

Fig. 3. Top: Comparison of $g_N(0)$ as function of N (solid line) to the true value $(\gamma|_{\partial\Omega} * \eta^2)(0)$ (dotted line). Bottom: Comparison of $h_N(0)$ as function of N (solid line) to the true value $(\partial\gamma/\partial r|_{\partial\Omega} * \eta^2)(0)$ (dotted line)

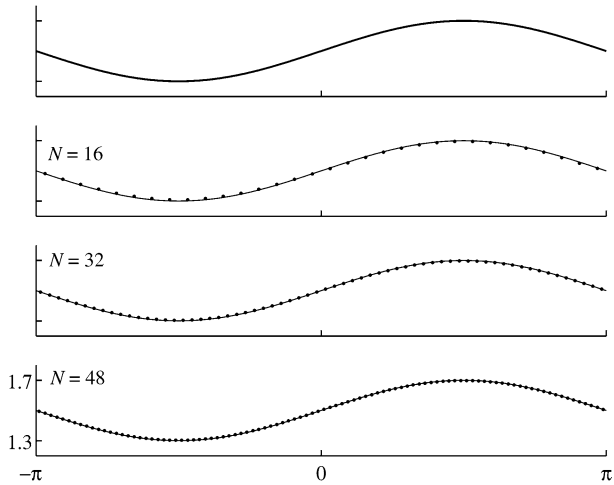

Fig. 4. Results for the simulated human chest phantom. Top plot: The trace $\gamma|_{\partial\Omega}$ as function of θ (thick line) and the convolution $(\gamma|_{\partial\Omega} * \eta^2)(\theta)$ (thin line). The graphs are so close together that they cannot be distinguished. Other plots: the function $\tilde{g}_N(\theta)$ (dots) computed from data with 0.01% noise, and $(\gamma|_{\partial\Omega} * \eta^2)(\theta)$. In all plots, the axis limits are the same

For quantitative assessment of the reconstruction error, we define

$$E_g^2(N) = \frac{\|\tilde{g}_N - \gamma * \eta^2\|_{L^2(\partial\Omega)}}{\|\gamma\|_{L^2(\partial\Omega)}}, \qquad E_g^\infty(N) = \frac{\max_{\partial\Omega} |\tilde{g}_N - \gamma * \eta^2|}{\max_{\partial\Omega} |\gamma|}. \tag{4.2}$$

Further, we define errors $E_h^2(N)$ and $E_h^\infty(N)$ by replacing $\tilde{g}$ with $\tilde{h}$ and γ with $\partial\gamma/\partial r$ in (4.2). See Table 1 for reconstruction errors.

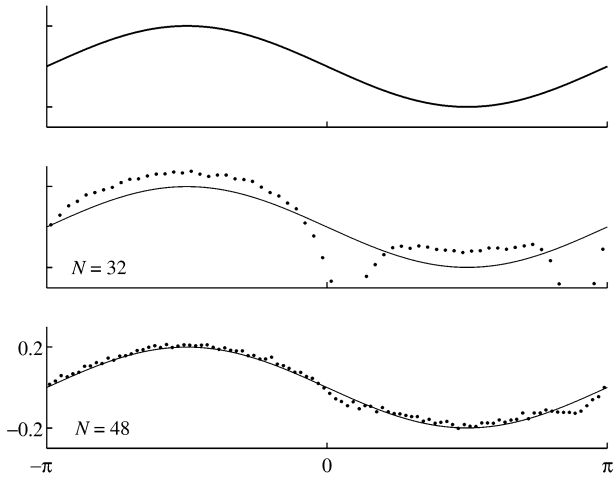

Fig. 5. Results for the simulated human chest phantom. Top plot: The normal derivative $\partial\gamma/\partial r|_{\partial\Omega}$ as function of θ (thick line) and the convolution $(\partial\gamma/\partial r|_{\partial\Omega} * \eta^2)(\theta)$ (thin line). The graphs are so close together that they cannot be distinguished. Other plots: The function $\tilde{h}_N(\theta)$ (dots) computed from data with 0.01% noise, and $(\partial\gamma/\partial r|_{\partial\Omega} * \eta^2)(\theta)$. In all plots, the axis limits are the same

Table 1. Left: Relative errors for the reconstruction of $\gamma|_{\partial\Omega}$ and $\partial\gamma/\partial\Omega|_{\partial\Omega}$ from noisy data with various N. For definitions of $E_g^2(N)$ and $E_g^\infty(N)$ see (4.2)

N	$E_g^2(N)$	$E_g^\infty(N)$	$E_h^2(N)$	$E_h^\infty(N)$
16	0.003	0.005	22.51	19.41
32	0.001	0.002	0.95	2.10
48	0.001	0.001	0.14	0.29

4.2. Smooth Conductivity with Rapid Changes

We define a smooth conductivity γ' on the unit disc by the following formula:

$$\gamma'(x_1, x_2) = 2 + \frac{2}{10}\sum_{\ell=1}^{10}(-1)^\ell Re(z^{2\ell}),$$

where $z = x_1 + ix_2$. See the middle plot of Fig. 1. The trace and normal derivative of γ' oscillate so rapidly that there is a significant difference between the actual functions and convolved ones. Quantitatively, the relative $L^2(\partial\Omega)$ and $L^\infty(\partial\Omega)$ errors between them are the following:

$$\frac{\|\gamma' - \gamma' * \eta^2\|_{L^2(\partial\Omega)}}{\|\gamma'\|_{L^2(\partial\Omega)}} \approx 0.09, \qquad \frac{\|\partial\gamma'/\partial r - (\partial\gamma'/\partial r) * \eta^2\|_{L^2(\partial\Omega)}}{\|\partial\gamma'/\partial r\|_{L^2(\partial\Omega)}} \approx 0.17,$$

$$\frac{\max_{\partial\Omega}|\gamma' - \gamma' * \eta^2|}{\max_{\partial\Omega}|\gamma'|} \approx 0.58, \qquad \frac{\max_{\partial\Omega}|\partial\gamma'/\partial r - (\partial\gamma'/\partial r) * \eta^2|}{\max_{\partial\Omega}|\partial\gamma'/\partial r|} \approx 0.48.$$

We compute g'_N with formula (3.2) and h'_N with formula (3.6) for $N = 16, 32, 48$. See Figs. 6 and 7 for the results.

Similarly to (4.2) we define

$$E^2_{g'}(N) = \frac{\|g'_N - \gamma * \eta^2\|_{L^2(\partial\Omega)}}{\|\gamma\|_{L^2(\partial\Omega)}}, \qquad E^\infty_{g'}(N) = \frac{\max_{\partial\Omega} |g'_N - \gamma * \eta^2|}{\max_{\partial\Omega} |\gamma|}. \tag{4.3}$$

See Table 2 for reconstruction errors.

4.3. Discontinuous Conductivity

We define a discontinuous conductivity γ'' on the unit disc:

$$\gamma''(x_1, x_2) = 2 + \frac{1}{2}\sqrt{x_1^2 + x_2^2}\arctan\frac{x_2}{x_1} \quad .$$

See the right plot of Fig. 1. The two points of discontinuity yield a significant difference between the actual functions and convolved ones. Quantitatively, the relative $L^2(\partial\Omega)$ and $L^\infty(\partial\Omega)$ errors between them are the following:

$$\frac{\|\gamma'' - \gamma'' * \eta^2\|_{L^2(\partial\Omega)}}{\|\gamma''\|_{L^2(\partial\Omega)}} \approx 0.06, \qquad \frac{\|\partial\gamma''/\partial r - (\partial\gamma''/\partial r) * \eta^2\|_{L^2(\partial\Omega)}}{\|\partial\gamma''/\partial r\|_{L^2(\partial\Omega)}} \approx 0.26,$$

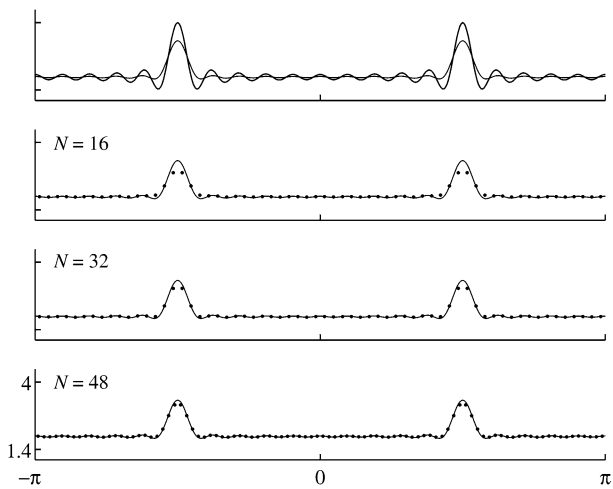

Fig. 6. Results for the smooth conductivity with rapid changes. Top plot: The trace $\gamma'|_{\partial\Omega}$ as function of θ (thick line) and the convolution $(\gamma'|_{\partial\Omega} * \eta^2)(\theta)$ (thin line). Other plots: the function $g'_N(\theta)$ (dots) computed from non-noisy data and $(\gamma'|_{\partial\Omega} * \eta^2)(\theta)$. In all plots, the axis limits are the same

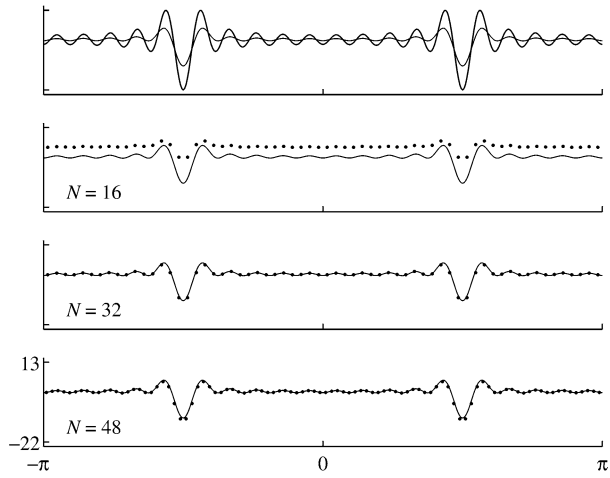

Fig. 7. Results for the smooth conductivity with rapid changes. Top plot: The normal derivative $\partial\gamma'/\partial r|_{\partial\Omega}$ as function of θ (thick line) and the convolution $(\partial\gamma'/\partial r|_{\partial\Omega} * \eta^2)(\theta)$ (thin line). Other plots: $h'_N(\theta)$ (dots) computed from non-noisy data and $(\partial\gamma'/\partial r|_{\partial\Omega} * \eta^2)(\theta)$. In all plots, the axis limits are the same

Table 2. Left: Relative errors for the reconstruction of $\gamma'|_{\partial\Omega}$ and $\partial\gamma'/\partial\Omega|_{\partial\Omega}$ from noisy data with various N. For definitions of $E^2_{g'}(N)$ and $E^\infty_{g'}(N)$, see formula

N	$E^2_{g'}(N)$	$E^\infty_{g'}(N)$	$E^2_{h'}(N)$	$E^\infty_{h'}(N)$
16	0.04	0.09	0.85	0.56
32	0.02	0.04	0.06	0.05
48	0.01	0.03	0.08	0.07

$$\frac{\max_{\partial\Omega}|\gamma'' - \gamma'' * \eta^2|}{\max_{\partial\Omega}|\gamma''|} \approx 0.58, \qquad \frac{\max_{\partial\Omega}|\partial\gamma''/\partial r - (\partial\gamma''/\partial r) * \eta^2|}{\max_{\partial\Omega}|\partial\gamma''/\partial r|} \approx 0.48.$$

We compute g''_N with formula (3.2) and h''_N with formula (3.6) for $N = 16, 32, 48$. See Figs. 8 and 9 for the results. See Table 3 for reconstruction errors.

5. Discussion

We presented a numerical implementation of the weak-form reconstruction of the trace and normal derivative of a smooth conductivity from the localized DN map. We demonstrated the algorithm with three example conductivities.

The first example was a simulated cross-section of the human chest. The conductivity was reconstructed with reasonable accuracy from simulated noisy EIT measurements with 32 or more electrodes and noise level 0.01%. Normal derivative could not be recovered using 32 or 64 electrodes with acceptable accuracy, but reconstruction from 96-electrode measurements had 14% relative L^2 error. Reconstruction of normal derivative is especially difficult near parameter values

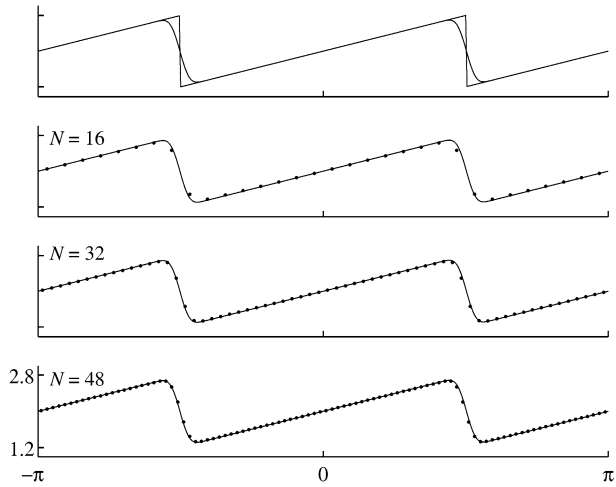

Fig. 8. Results for the discontinuous conductivity. Top plot: The trace $\gamma''|_{\partial\Omega}$ as function of θ (thick line) and the convolution $(\gamma''|_{\partial\Omega} * \eta^2)(\theta)$ (thin line). Other plots: the function $g''_N(\theta)$ (dots) computed from non-noisy data and $(\gamma''|_{\partial\Omega} * \eta^2)(\theta)$. In all plots, the axis limits are the same

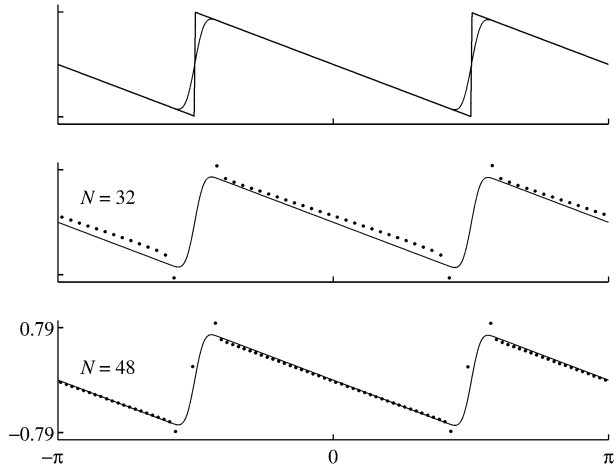

Fig. 9. Results for the discontinuous conductivity. Top plot: The normal derivative $\partial\gamma''/\partial r|_{\partial\Omega}$ as function of θ (thick line) and the convolution $(\partial\gamma''/\partial r|_{\partial\Omega} * \eta^2)(\theta)$ (thin line). Other plots: the function $h''_N(\theta)$ (dots) computed from non-noisy data and $(\partial\gamma''/\partial r|_{\partial\Omega} * \eta^2)(\theta)$ (thin line). In all plots, the axis limits are the same

Table 3. Left: Relative errors for the reconstruction of $\gamma''|_{\partial\Omega}$ for $N = 16, 32, 48$ corresponding to electrode configurations with 32, 64 and 96 electrodes, respectively. The errors $E^2_{g''}(N)$ and $E^\infty_{g''}(N)$ are defined by an obvious modification of (4.3). Right: errors for the reconstruction of $\partial\gamma''/\partial\Omega|_{\partial\Omega}$

N	$E^2_{g''}(N)$	$E^\infty_{g''}(N)$	$E^2_{h''}(N)$	$E^\infty_{h''}(N)$
16	0.02	0.05	10.1	7.8
32	0.01	0.03	1.6	4.0
48	0.01	0.03	1.3	3.5

$\theta = 0$ and $\theta = \pi$. This may due to a discontinuity (boundary of lung) being close to the surface at those points; analysis of this phenomenon requires further study.

The second example was a simulated smooth conductivity with rapidly changing features at the boundary. The weak-form reconstruction leads to expected error of relative L^2 magnitude 9% in the reconstruction due to the convolution with a point spread function. The blurred trace can be reconstructed from non-noisy data with 4% relative L^2 errors using 32 electrodes and with 2% error with 64 or more electrodes. For successful recovery of the blurred normal derivative from non-noisy data, 32 electrodes is not enough but 64 seems to suffice.

The third example was chosen to be piecewise smooth and to have discontinuities both in trace and normal derivative. We found that the presented approach works well away from the points of discontinuity (as predicted by the theory) and recovers an approximation of the trace near the discontinuities. For the trace, the relative L^2 error in the reconstruction from non-noisy data was at most 2%, suggesting that the reconstruction formula may be proven to cover the discontinuous case. However, the reconstruction formula for the normal derivative fails near points of discontinuity.

In conclusion, the results suggest that formulae (1.3) and (1.4) can be used for approximately recovering the trace and normal derivative of a smooth conductivity from local EIT measurements with at least 32 and 96 electrodes, respectively. However, the practical value of our results needs to be verified with a future study using measured data and adequate modelling for electrodes.

Acknowledgements

The authors thank the anonymous referees for their constructive comments on the manuscript. SS was supported by Japan Society for the Promotion of Science (JSPS) Grant-in-Aid for Postdoctoral Fellows (No. 00002757). KT was partially supported by Grant-in-Aid for Scientific Research (C) (No. 16540095), JSPS.

References

[1] Astala, K., Päivärinta, L.: Calderón's inverse conductivity problem in the plane. University of Helsinki Department of Mathematics, Preprint 370, September 2003.
[2] Borcea, L.: Electrical impedance tomography. Inverse Problems *18*, R99–R136 (2002).
[3] Borcea, L.: Addendum to "Electrical Impedance Tomography". Inverse Problems *19*, 997–998 (2002).
[4] Brown, B. H., Barber, D. C., Seagar, A. D.: Applied potential tomography: possible clinical applications. Clin. Phys. Physiol. Meas. *6*, 109–121 (1985).
[5] Brown, R. M.: Recovering the conductivity at the boundary from the Dirichlet to Neumann map: a pointwise result, J. Inverse Ill-posed Prob. *9*, 567–574 (2001).
[6] Brown, R. M., Uhlmann, G.: Uniqueness in the inverse conductivity problem for nonsmooth conductivities in two dimensions. Communications in Partial Differential Equations *22*, 1009–1027 (1997).
[7] Calderón, A. P.: On an inverse boundary value problem. In: Seminar on Numerical Analysis and its Applications to Continuum Physics. Soc. Brasileira de Matemàtica, pp. 65–73 (1980).
[8] Cheney, M., Isaacson, D., Newell, J. C.: Electrical impedance tomography. SIAM Rev. *41*, 85–101 (1999).
[9] Cheng, K.-S., Isaacson, D., Newell, J. C., Gisser, D. G.: Electrode models for electric current computed tomography. IEEE Trans. Biomed. Imaging, pp. 918–924 (1989).

[10] Hecht, F., Pironneau, O., Ohtsuka, K.: Freefem++ Manual, http://www.ann.jussieu.fr/ hecht/ freefem++.htm 2003.
[11] Isaacson, D., Mueller, J. L., Newell, J. C., Siltanen, S.: Reconstructions of chest phantoms by the d-bar method for electrical impedance tomography (submitted).
[12] Kang, H., Yun, K.: Boundary determination of conductivities and Riemannian metrics via local Dirichlet-to-Neumann operator. SIAM J. Math. Anal. *34*, 719–735 (2003).
[13] Knudsen, K.: On the inverse conductivity problem, Ph.D. thesis, Aalborg University (2002).
[14] Knudsen, K.: A new direct method for reconstructing isotropic conductivities in the plane. Physiol. Meas. *24*, 391–401 (2003).
[15] Knudsen, K., Tamasan, A.: Reconstruction of less regular conductivities in the plane, MSRI Preprint 2001–035 (2001).
[16] Mueller, J. L., Siltanen, S.: Direct reconstructions of conductivities from boundary measurements. SIAM J. Sci. Comput. *24*, 1232–1266 (2003).
[17] Nachman, A. I.: Global uniqueness for a two-dimensional inverse boundary value problem. Ann. Math. *143*, 71–96 (1996).
[18] Nakamura, G., Tanuma, K.: Local determination of conductivity at the boundary from the Dirichlet-to-Neumann map. Inverse Problems *17*, 405–419 (2001).
[19] Nakamura, G., Tanuma, K.: Direct determination of the derivatives of conductivity at the boundary from the localized Dirichlet to Neumann map. Comm. Korean Math. Soc. *16*, 415–425 (2001).
[20] Nakamura, G., Tanuma, K.: Formulas for reconstructing conductivity and its normal derivative at the boundary from the localized Dirichlet to Neumann map. In: Recent Development in Theories and Numerics. Int. Conf. on Inverse Problems (Yiu-Chung Hon, Masahiro Yamamoto, Jin Cheng, June-Yub Lee, eds.), pp. 192–201, World Scientific 2003.
[21] Nakamura, G., Tanuma, K.: Formulas for reconstructing conductivity and its normal derivative at the boundary from the localized Dirichlet to Neumann map (preprint).
[22] Siltanen, S., Mueller, J. L., Isaacson, D.: An implementation of the reconstruction algorithm of A. Nachman for the 2-D inverse conductivity problem. Inverse Problems *16*, 681–699 (2000).
[23] Somersalo, E., Cheney, M., Isaacson, D.: Existence and uniqueness for electrode models for electric current computed tomography. SIAM J. Appl. Math. *52*, 1023–1040 (1992).
[24] Sylvester, J., Uhlmann, G.: Inverse boundary value problem at the boundary-continuous dependence. Comm. Pure Appl. Math. *61*, 197–219 (1988).
[25] Vogel, C.: Computational methods for inverse problems. SIAM (2002).

G. Nakamura
Graduate School of Science
Hokkaido University
Sapporo 060-0810
Japan
e-mail: gnaka@math.sci.hokudai.ac.jp

K. Tanuma
Gunma University
Department of Mathematics
Tenjin-cho 1-5-1, 376-8515 Kiryu
Japan
e-mail: tanuma@sv1.math.sci.gunma-u.ac.jp

S. Siltanen
Instrumentarium Imaging
(part of GE Healthcare)
P.O. Box 20
04301 Tuusula
Finland
e-mail: samuli.siltanen@iki.fi

S. Wang
Graduate School of Science
Hokkaido University
Sapporo 060-0810
Japan
e-mail: wang@math.sci.hokudai.ac.jp